OPEN ACCESS



Nonneutralized Electric Currents as a Proxy for Eruptive Activity in Solar Active Regions

Y. Liu¹, T. Török², V. S. Titov², J. E. Leake³, X. Sun (孙旭东)⁴, and M. Jin⁵, W.W. Hansen Experimental Physics Laboratory, Stanford University, Stanford, CA 94305-4085, USA; yliu@sun.stanford.edu Predictive Science Inc., 9990 Mesa Rim Road, Suite 170, San Diego, CA 92121, USA NASA Goddard Space Flight Center, Greenbelt, MD 20771, USA Institute for Astronomy, University of Hawai'i at Mānoa, Pukalani, HI 96768, USA Lockheed Martin Solar and Astrophysics Lab, Palo Alto, CA 94304, USA Received 2022 June 13; revised 2023 November 20; accepted 2023 December 2; published 2024 January 22

Abstract

It has been suggested that the ratio of photospheric direct to return current, |DC/RC|, may be a better proxy for assessing the ability of solar active regions to produce a coronal mass ejection (CME) than others such as the amount of shear along the polarity inversion line (PIL). To test this conjecture, we measure both quantities prior to eruptive and confined flares of varying magnitude. We find that eruptive-flare source regions have |DC/RC| > 1.63 and PIL shear above 45° (average values of 3°.2 and 68°, respectively), tending to be larger for stronger events, while both quantities are on average smaller for confined-flare source regions (2°.2 and 68°, respectively), albeit with substantial overlap. Many source regions, especially those of eruptive X-class flares, exhibit elongated direct currents (EDCs) bracketing the eruptive PIL segment, which typically coincide with areas of continuous PIL shear above 45°. However, a small subset of confined-flare source regions have |DC/RC| close to unity, very low PIL shear (<38°), and no clear EDC signatures, rendering such regions less likely to produce a CME. A simple quantitative analysis reveals that |DC/RC| and PIL shear are almost equally good proxies for assessing CME-productivity, comparable to other proxies suggested in the literature. We also show that an inadequate selection of the current-integration area typically yields a substantial underestimation of |DC/RC|, discuss specific cases that require careful consideration for |DC/RC| calculation and interpretation of the results, and suggest improving photospheric CME-productivity proxies by incorporating coronal measures such as the decay index.

Unified Astronomy Thesaurus concepts: Solar activity (1475); Solar magnetic fields (1503); Solar coronal mass ejections (310); Solar flares (1496); Solar photosphere (1518)

1. Introduction

Large-scale solar eruptions are sudden disruptions of portions of the magnetic field in the solar corona, with the strongest events typically occurring in active regions (ARs). They always originate over polarity inversion lines (PILs) and are observed as prominence eruptions, flares, and coronal mass ejections (CMEs). The largest events typically include all three manifestations ("eruptive flares"), but flares, even very strong ones, can occur also without a CME or full prominence eruption ("confined flares"). The energy required to power solar eruptions is stored as so-called free magnetic energy in currentcarrying magnetic fields (e.g., Forbes 2000; Schrijver 2009; Green et al. 2018), which are most likely organized in the form of magnetic flux ropes (MFRs) or highly sheared magnetic arcades (SMAs; see Patsourakos et al. 2020 for a detailed discussion). It is well established that solar eruptions, especially CMEs, are the main driver of space-weather disturbances close to the Earth (e.g., Temmer 2021; Zhang et al. 2021). Accordingly, a large body of research has been devoted to determining AR characteristics that would allow one to predict the occurrence of eruptions (at least in a probabilistic manner; see, e.g., the recent review by Kontogiannis 2023). Along with quantities such as the total AR flux, specific interest has been paid to the location and amount of magnetic shear along PILs,

Original content from this work may be used under the terms of the Creative Commons Attribution 4.0 licence. Any further distribution of this work must maintain attribution to the author(s) and the title of the work, journal citation and DOI.

as this quantity is commonly regarded as a proxy for the free magnetic energy, and since strongly sheared PILs are often associated with eruptive activity (e.g., Schrijver 2009). Some of these works considered flares in general (see, e.g., the evaluation of prediction schemes in Barnes et al. 2016), while others focused on CMEs (e.g., Falconer et al. 2008); see also Kazachenko et al. (2022a) for a summary of recent investigations addressing the statistical properties of confined and eruptive flares.

In a recent study, Liu et al. (2017) suggested that the ratio of the total direct and return current measured at the photosphere, |DC/RC|, can be used to assess the *ability* of an AR to produce an eruptive flare (i.e., a CME) and that this quantity may be better suited for this purpose than the amount of shear along the PIL. We note that DCs bracketing a PIL also are a signature of nonpotential fields in the low corona, so they should exhibit some correlation with the PIL shear (e.g., Kazachenko et al. 2022b). However, this is a priori not clear for |DC/RC|, as the value of this quantity depends also on the potential presence and strength of RCs surrounding the DC (see Section 4 for a discussion). By averaging |DC/RC| for a time period of several days, Liu et al. (2017) demonstrated that the core-field regions of CME-producing ARs are characterized by |DC/RC| ratios significantly larger than unity, while quiet (nonflaring) ARs, as well as ARs that produce only confined flares, are characterized by |DC/RC| values close to unity. The differences in the PIL shear between eruptive and noneruptive ARs, on the other hand, appeared less pronounced. However, this study was based on a very small sample of only four ARs, where two ARs produced strong (M3 or larger) eruptive flares, one produced only strong confined flares in its central area, and one did not produce any flares above C-class.

The motivation for using |DC/RC| as a proxy for potential CME occurrence stems from the idea that the source regions of eruptive flares are characterized by substantial net currents (i.e., |DC| is significantly larger than |RC|). While it has been debated whether ARs can carry such currents in the first place (see Liu et al. 2017 and references therein), recent observational studies of individual ARs have found current neutralization at the photospheric level for quiet regions, and strong net currents for highly eruptive ones (e.g., Ravindra et al. 2011; Georgoulis et al. 2012; Vemareddy et al. 2015, who considered one, two, and one case(s), respectively). The presence of strong net currents was also found in idealized numerical simulations of AR formation for cases where substantial shear developed along the PIL (e.g., Török & Kliem 2003; Török et al. 2014; Dalmasse et al. 2015).

The origin of nonneutralized currents as seen in the photosphere is not entirely clear, as magnetic flux tubes rising in the convection zone are believed to be magnetically isolated, i.e., current-neutralized. Longcope & Welsch (2000) suggested that the return current of an emerging tube may be "trapped" at the surface, and this has indeed been found in the flux-emergence simulation analyzed in Török et al. (2014). Recently, Sun & Cheung (2021) showed that for a subsurface flux tube with neutralized toroidal (axial) current, the poloidal (azimuthal) current can generate a significant nonneutralized component when projected onto the vertical direction (i.e., onto the photosphere). Their simple model does not incorporate the highly complex process of flux emergence, though, therefore it cannot predict the resulting current distribution in the corona.

The quantity |DC/RC| has been measured by several authors for individual ARs and flares, as well as for extended samples. For example, Qiu et al. (2020) found $|DC/RC| \approx 1.4$ before an eruptive flare that occurred on 2015 March 11 in NOAA AR 12297. Vemareddy (2019) studied the evolution of 20 ARs over several days and found that the CME-producing ARs had peak |DC/RC| values between 1.2 and 2.0, while quiet and flaring ARs (without CMEs) all had peak values below 1.2. Avallone & Sun (2020) considered a sample of 15 quiet, 11 CME-producing, and 4 flaring ARs. Considering |DC/RC| on the day of the eruption, or after 80 percent of the flux has emerged (for quiet ARs), they found that quiet and flaring ARs had |DC/RC| values close to unity, with some exceptions (the largest value being 1.31), while CME-producing ARs had significantly larger numbers, between 1.11 and 2.15.

In contrast, considering a sample of 71 two-ribbon flares, He et al. (2020) concluded that the degree of current neutralization cannot be used to distinguish between confined and eruptive events. Performing a detailed study of the properties of 40 flares, Kazachenko et al. (2022b) reported |DC/RC| > 2 for two confined flares, and values close to unity for some eruptive flares (see Sections 3.3 and 3.5 for a discussion of such cases). Overall, however, their results are in line with the trends found by Vemareddy (2019) and Avallone & Sun (2020), namely, that CME-producing ARs tend to have larger values of |DC/RC| than flaring or quiet ARs.

It is important to note that these studies used different area selections for integrating the photospheric electric currents to obtain |DC/RC|. Vemareddy (2019) chose a rectangular area surrounding the whole AR, including only pixels above a total

field strength of 200 G. Avallone & Sun (2020) did the same for well-isolated ARs, but used a manually selected subregion, based on EUV observations of the flare (presumably also rectangular), for complex or not well-isolated ARs. He et al. (2020), on the other hand, considered only currents that were located within the area of the flare ribbons. Kazachenko et al. (2022b) used three methods to measure |DC/RC|, namely, for entire AR polarities, the cumulative flare-ribbon area, and a narrow area surrounding the PIL (with a width of approximately 10 HMI pixels). They found that, in general, |DC/RC| increases as one decreases the integration area from the whole AR polarity to the flare-ribbon area and further to the PIL area.

These different choices of the integration area likely explain some contradictory results regarding the relation between |DC/RC| and the average PIL shear. For example, while Kazachenko et al. (2022b) found a strong correlation between |DC/RC| and PIL shear when integrating the former over the cumulative ribbon area, Avallone & Sun (2020), albeit noting that CME-producing ARs have higher PIL shear than CME-quiet ones, did not find a clear correlation.

As pointed out by Liu et al. (2017), the obtained |DC/RC|value can strongly depend on the selected integration area. Generally, one should aim to perform the integration over the area of the (potentially) erupting flux and avoid contributions from areas that are irrelevant to the eruption. This is especially true for large and complex ARs, where the erupting flux may cover only a relatively small fraction of the total AR flux. On the other hand, integrating the current density only over a (narrow) stripe around the PIL will typically exclude a substantial fraction of the eruptive flux. Integrating it over the ribbon area takes into account only flux that reconnects across the flare current sheet. However, this does not necessarily cover the entire erupting current-carrying flux, as parts of it may never get involved in the flare reconnection, again potentially leading to "wrong" |DC/RC| values, which may explain the seemingly different results by He et al. (2020). Moreover, some (typically thinner and weaker) flare ribbons may result from the perturbation of adjacent quasi-separatrix layers (OSLs) that are not part of the erupting flux (e.g., Masson et al. 2009).

In order to capture the erupting (or potentially erupting) flux more accurately, in Liu et al. (2017) we employed nonlinear force-free field (NLFFF) extrapolations to calculate maps of the squashing factor (Titov 2007; Titov et al. 2011). Those were then used, aided by visual inspection of selected field lines, to determine the integration area by deriving a "mask" that encloses the region of closed flux above an eruptive PIL segment (see also Section 2.2). We demonstrated, for AR 11158, that |DC/RC| is indeed significantly larger if the integration is performed within such a mask ("mask method" hereafter), compared to manually choosing a rectangular area that includes the entire AR ("area method" hereafter), as done in some of the works cited above.

In this research, we extend our previous study in Liu et al. (2017) by including a larger sample of ARs and eruptions, in order to further investigate the relationship between the degree of current neutralization, the amount of PIL shear, and the eruptive activity of ARs. The sample includes ARs that produced strong and moderate eruptive flares, as well as confined flares, in the time period from 2011 February to 2017 September. We pay particular attention to the role of the integration area for the calculation of |DC/RC|, and we discuss

Table 1
Ratio of the Total Direct to Total Return Current, |DC/RC|, and Magnetic Shear along the PIL for Strong Flares (X and M Class) with and without CMEs and for Weak Flares with CMEs (See Text for Details)

| AR | Date and Time | Flare/ CME | Position | $ DC/RC ^+ B_z > 0$ | $ DC/RC ^- B_z < 0$ | DC/RC mean | Shear (deg) | EDC |
|-------------|-------------------|---------------|----------|----------------------|----------------------|-------------------|----------------|-----|
| Group 1 | | | | | | | | |
| 11158* | 2011.02.15, 01:44 | X2.2 Y | S21W10 | 2.841 ± 0.060 | 3.378 ± 0.094 | 3.110 ± 0.380 | 75.9 ± 1.7 | Y |
| 11283 | 2011.09.06, 22:12 | X2.1 Y | N14W18 | 3.602 ± 0.142 | 4.650 ± 0.255 | 4.126 ± 0.741 | 73.4 ± 0.2 | Y |
| 11429* | 2012.03.07, 00:02 | X5.4 Y | N17E24 | 2.567 ± 0.048 | 2.560 ± 0.038 | 2.564 ± 0.031 | 74.0 ± 0.1 | Y |
| 11515 | 2012.07.06, 23:01 | X1.1 Y | S17W50 | 4.670 ± 0.199 | 4.722 ± 0.270 | 4.696 ± 0.168 | 81.3 ± 0.7 | Y |
| 11520 | 2012.07.12, 15:37 | X1.4 Y | S17W08 | 2.770 ± 0.070 | 2.652 ± 0.058 | 2.711 ± 0.083 | 60.8 ± 0.1 | ? |
| 11890 | 2013.11.05, 22:07 | X3.3 Y | S09E36 | 6.267 ± 0.339 | 7.716 ± 0.337 | 6.992 ± 1.024 | 73.1 ± 0.5 | Y |
| 12017 | 2014.03.29, 17:35 | X1.0 Y | N10W32 | 2.299 ± 0.069 | 2.308 ± 0.070 | 2.304 ± 0.049 | 60.5 ± 0.3 | Y |
| 12158 | 2014.09.10, 17:21 | X1.6 Y | N15E02 | 2.114 ± 0.052 | 2.519 ± 0.070 | 2.317 ± 0.286 | 63.1 ± 0.4 | ? |
| 12205 | 2014.11.07, 16:53 | X1.6 Y | N15E33 | 3.498 ± 0.091 | 2.617 ± 0.057 | 3.058 ± 0.623 | 74.7 ± 0.4 | Y |
| 12242^{+} | 2014.12.20, 00:11 | X1.8 Y | S18W29 | 2.165 ± 0.039 | 2.390 ± 0.052 | 2.278 ± 0.159 | 67.9 ± 0.3 | Y |
| 12297 | 2015.03.11, 16:11 | X2.1 Y | S16E13 | 5.120 ± 0.193 | 2.360 ± 0.058 | 3.740 ± 1.952 | 68.8 ± 1.3 | Y |
| 12673 | 2017.09.06, 11:53 | X9.3 Y | S09W38 | 6.683 ± 0.149 | 4.530 ± 0.095 | 5.607 ± 1.522 | 73.8 ± 6.0 | Y |
| Group 2 | | | | | | | | |
| 11166+ | 2011.03.07, 13:45 | M1.9 Y | N11E13 | 1.885 ± 0.121 | 1.547 ± 0.043 | 1.716 ± 0.239 | 51.2 ± 3.8 | N |
| 11261 | 2011.08.02, 05:19 | M1.4 Y | N16W08 | 3.781 ± 0.144 | 3.194 ± 0.113 | 3.488 ± 0.415 | 70.0 ± 0.1 | Y |
| 11305 | 2011.10.02, 00:37 | M3.9 Y | N11W12 | 3.135 ± 0.123 | 3.113 ± 0.124 | 3.124 ± 0.087 | 70.1 ± 0.2 | ? |
| 11667 | 2013.02.06, 00:04 | C8.7 Y | N22E14 | 1.767 ± 0.098 | 1.513 ± 0.095 | 1.640 ± 0.180 | ••• | N |
| 11817 | 2013.08.12, 10:21 | M1.5 Y | S22E14 | 2.992 ± 0.104 | 2.654 ± 0.081 | 2.823 ± 0.239 | 46.1 ± 2.8 | Y |
| 12027 | 2014.04.04, 13:34 | C8.3 Y | N13E23 | 1.978 ± 0.218 | 1.527 ± 0.094 | 1.753 ± 0.319 | ••• | N |
| Group 3 | | | | | | | | |
| 11166^{+} | 2011.03.09, 23:13 | X1.5 N | N11W15 | 1.026 ± 0.020 | 1.153 ± 0.017 | 1.090 ± 0.090 | 37.1 ± 2.6 | ? |
| 11476 | 2012.05.10, 04:11 | M5.7 N | N13E22 | 4.152 ± 0.174 | 6.665 ± 0.324 | 5.408 ± 1.777 | 63.1 ± 1.2 | Y |
| 11520 | 2012.07.10, 04:58 | M1.7 N | S17E27 | 2.294 ± 0.062 | 2.836 ± 0.065 | 2.565 ± 0.383 | 49.9 ± 2.9 | Y |
| 11875 | 2013.10.24, 09:59 | M2.5 N | N06W14 | 1.893 ± 0.048 | 1.727 ± 0.047 | 1.810 ± 0.117 | 48.2 ± 3.9 | ? |
| 11967 | 2014.02.04, 03:57 | M5.2 N | S16W06 | 3.019 ± 0.045 | 2.256 ± 0.045 | 2.638 ± 0.540 | 46.9 ± 1.7 | Y |
| 12192* | 2014.10.24, 21:07 | X3.1 N | S14E15 | 1.036 ± 0.011 | 1.005 ± 0.010 | 1.021 ± 0.022 | 26.5 ± 1.4 | N |
| 12222 | 2014.12.04, 18:05 | M6.1 N | S20W32 | 1.085 ± 0.022 | 1.044 ± 0.024 | 1.065 ± 0.029 | 26.1 ± 6.2 | ? |
| 12242^{+} | 2014.12.19, 09:31 | M1.3 N | S18W23 | 1.148 ± 0.029 | 1.162 ± 0.028 | 1.155 ± 0.020 | 32.5 ± 0.5 | N |
| 12268 | 2015.01.29, 11:32 | M2.1 N | S12W06 | 2.861 ± 0.155 | 2.947 ± 0.205 | 2.904 ± 0.104 | 75.7 ± 0.4 | ? |
| 12422 | 2015.09.28, 14:53 | M7.6 N | S20W16 | 1.978 ± 0.041 | 2.182 ± 0.061 | 2.080 ± 0.144 | 57.5 ± 3.8 | Y |

Note. ARs that produced events in *different* source regions (PIL segments) are marked with a plus sign; ARs that were investigated also in Liu et al. (2017) are marked with an asterisk. EDC stands for "Elongated Direct Current," i.e., the presence of a (often double-*J*-shaped) pattern of an elongated, coherent direct-current concentration bracketing the PIL ("Y," "N," and "?" stand for yes, no, and ambiguous, respectively).

peculiar cases such as the presence of closely packed PILs and the absence of pronounced current signatures at the photosphere. This article is organized as follows. In Section 2, we describe our sample, the data we used, and the methodology of our analysis. In Section 3, we present our results and discuss a number of aspects that may lead to an improper analysis or interpretation of the results. Finally, we present a summary and discussion in Section 4.

2. Data and Methodology

2.1. Data

In contrast to Liu et al. (2017), who averaged |DC/RC| over an extended time period for four ARs, we here obtain the |DC/RC| value prior to a specific event, which allows for a more accurate characterization of the relation between this quantity and eruptive activity. To this end, we select a representative sample of 28 flares that we group based on their magnitude, and on whether or not they were associated with a CME (Table 1). Since our study focuses on the properties of the underlying source region, we selected only flares from different source regions. The only exception is AR 11520, where the source region evolved significantly between the two flares considered. Group 1 contains 12 strong eruptive

flares of X-class from 12 different ARs; Group 2 contains six medium eruptive flares of high C-class (\geqslant C8.3) and low-to-average M class (M1.5–M3.9) from six different ARs; and Group 3 contains 10 medium-to-strong confined flares of M and X-class (M1.3–X3.1) from 10 different ARs. Note that three ARs (11166, 11520, and 12242) are present with one eruptive and one confined flare each.

To select ARs and events for Groups 1 and 3, we evaluated all X-class flares in the time period ranging from 2010 to 2017 for which HMI observations are available. We found 28 ARs that produced X-class flares during this period, out of which we selected 12 ARs that produced an event associated with a CME and two ARs that produced a confined event. These include three ARs (11158, 11429, and 12192) that were analyzed in Liu et al. (2017). The remaining ARs only produced X-class events that occurred relatively close to the limb ($>50^{\circ}$ from the central meridian) or were located in relatively weak fields outside of the AR (such as the 2014 January 7 event, which we discuss in Section 3.5). The HMI vector data are less reliable in such cases, so we excluded them from our sample. For ARs that produced multiple X-class flares, we chose the event that occurred closest to the central meridian. Since we found only two ARs with confined X-class flares that were close enough to the disk center, we added eight confined flares of M class to Group 3. Two

events (M1.7 in AR 11520 and M1.3 in AR 12242) were studied in Li et al. (2020). The remaining six events were chosen from the database in Li et al. (2022), which lists 63 confined $M \geqslant 1.0$ flares (2010 June–2019 June) from ARs that either produced only confined flares or only eruptive flares (with one exception allowed for each case). We chose all the confined-event ARs from the database. For each chosen AR (11476, 11875, 11967, 12222, 12268, and 12422), we select the strongest flare for our analysis, except for AR 11875, where the strongest flare (M3.5 on 2013 October 24, at 10:30 UT) occurred only 13 minutes after the end of another confined M2.5 flare. We therefore selected the latter event for our sample.

For Group 2, we searched for candidates by considering ARs that produced only relatively weak eruptive flares during their disk passage. We considered only events greater than the C5.0 class for an easier determination of their association with a CME. In total, we found six ARs that satisfied our criteria. According to the database in Li et al. (2022), AR 11261 produced three eruptive flares of M1.4, M6.0, and M 9.3 strength between August 2 and 4 in 2011. For our sample, we chose the M1.4 event to comply with our requirement of selecting only low-to-average M-class flares for this group. AR 11305 produced a number of eruptive C-class and M-class flares, of which we selected only the largest one (M3.9). AR 11667 produced one C8.4 and one C8.7 flare. The former took place at the limb and was therefore excluded. AR 11817 produced a C6.7, a C8.4, and an M1.5 flare (see Liu et al. 2016 for a detailed description). The C6.7 and C8.4 flares occurred 23 minutes apart, so we excluded the C6.7 event. AR 12027 produced an M6.5 and a C8.3 flare. The M6.5 event occurred 50° from the central meridian, so we selected only the C8.3 event. AR 11166 produces both eruptive and confined events, as did ARs 11520 and 12242 from Group 1. We discuss these ARs in detail in Section 3.3.

We note that our criterion of including only pixels with field strengths of at least 300 G (see Sections 2.2 and 2.3) restricted our determination of the PIL shear to four cases in Group 2. For the remaining two cases, the sections of the eruptive PIL segment that fulfill our criterion were too small to be considered as representative.

We use the Solar Dynamics Observatory's (SDO; Pesnell et al. 2012) Helioseismic and Magnetic Imager (HMI; Scherrer et al. 2012; Schou et al. 2012) vector magnetic-field data (Hoeksema et al. 2014) to calculate the electric current distribution and the PIL magnetic shear of the ARs prior to the respective events in our sample. HMI is a filtergraph instrument with full-disk coverage over 4096×4096 pixels. Its spatial resolution is about 1", with a 0."5 pixel size. The spectral line observed is the FeI 6173 Å absorption line formed in the photosphere (Norton et al. 2006). For vector magnetic-field measurements, it takes 135 s to obtain the filtergrams in six polarization states at six wavelength positions (90 s after 2016 April, when the observation mode changed). The Stokes parameters [I, O, U, V] are computed from those measurements and are further inverted to retrieve the vector magnetic field. In order to suppress the p-modes and increase the signal-to-noise ratio, usually the Stokes parameters are derived from filtergrams averaged over 1215 s using a cosine-apodized, moving-boxcar weighting with an FWHM of 720 s. Averages are computed at a 720 s cadence. They are then inverted to produce the vector magnetic field using the Very Fast Inversion of the Stokes Vector (VFISV) algorithm (Borrero et al. 2011; Centeno et al. 2014). The 180° degree ambiguity in the transverse-field

azimuth is resolved based on the "minimum energy" algorithm (Metcalf 1994; Leka et al. 2009). Photospheric patches containing ARs are automatically identified and bounded by a feature recognition model (Turmon et al. 2010), and the disambiguated vector magnetic-field data of ARs are deprojected to heliographic coordinates (Bobra et al. 2014). Here we use the Lambert (cylindrical equal area, CEA) projection method, centered on each region, for the remapping. The deprojected vector field data are then used for our computation.

2.2. Calculation of |DC/RC|

We employ the same approach as in Liu et al. (2017) to calculate the ratio of direct and return currents. For each case, the vertical electric current density, $J_z = \mu_0^{-1}(\frac{\partial By}{\partial x} - \frac{\partial Bx}{\partial y})$, is derived from the processed HMI vector magnetic-field data. In order to obtain the total direct and return current, positive and negative values of J_z are integrated separately. The direct current, DC, is defined as the current that connects the AR magnetic polarity centers, which for each polarity determines the sign of J_z to be used for its integration. The return current, RC, is then the integral over the values of J_z of the opposite sign for the same polarity. That is, $DC^{\pm} = \int J_z(\geq 0) ds$ and $RC^{\pm} = \int J_z(\leq 0) ds$ for $B_z \geq 0$ for an AR (or source region) with positive helicity. The ratio of the total direct current and return current, DC/RC, is computed for both polarities separately, i.e., we calculate the quantities $(DC/RC)^{\pm} = DC(B_z \geq 0)/RC(B_z \geq 0)$.

ARs, especially complex ones, often contain substantial noneruptive flux that is irrelevant to our investigation. Such flux may connect to other polarities of the AR, to neighboring ARs, or to remote areas on the Sun. As discussed in Section 3.1, selecting a too-widespread area for the current integration can lead to a significant underestimation of the relevant |DC/RC| value. Thus, to restrict our integration area as much as possible to the region of erupting flux, we select it via visual inspection of maps of the squashing factor Q (Titov 2007; Titov et al. 2011) and the observed locations of flare arcades and ribbons. We note that, while flare arcades and ribbons are only available after an eruption, Q-maps and fieldline connectivity obtained from magnetic-field extrapolations can be used also prior to a potential eruption to determine the area of closed flux over a PIL segment that may be prone to an eruption (see Liu et al. 2017). In most cases, this should provide a reasonably good proxy for the area of the erupting flux, as high-Q contours (separating different flux systems) have been shown to coincide relatively well with flare ribbons (e.g., Demoulin et al. 1997; Masson et al. 2009; Savcheva et al. 2015; Janvier et al. 2016; Vemareddy 2021).

Here we produce Q maps at a height of 3 Mm above the photosphere, using nonlinear force-free field (NLFFF) extrapolations (Wiegelmann 2004). We chose this height for two reasons. First, it greatly simplifies the Q-map by suppressing contributions from the many small-scale magnetic structures located at lower atmospheric heights. Second, the axis of a preeruptive MFR typically extends at least several Mm into the corona (e.g., Duan et al. 2019), so all of the closed flux overlying it will be captured.

Guided by the locations of flare arcades and (strong) ribbons in the AIA observations, we identify for each event segments of high-Q contours that enclose, or are co-spatial to, the area of erupted flux as suggested by the arcade/ribbon locations, and connect them to produce a mask (see Figure 1 and the

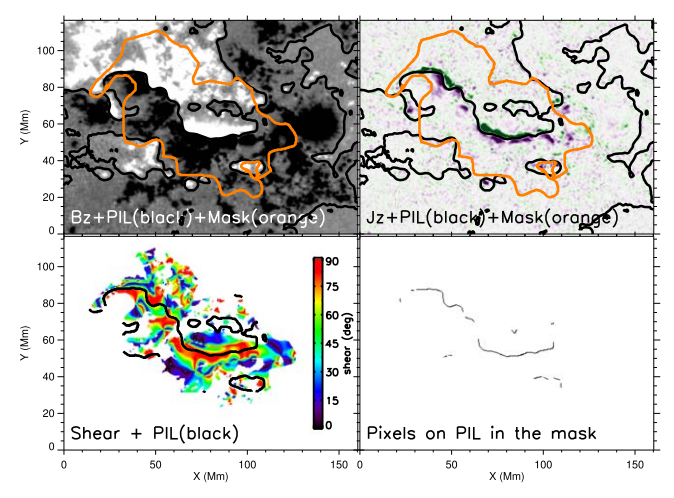


Figure 1. Top: Maps of B_z (left) and J_z (right) for AR 12205 at 15:00 UT on 2014 November 7, before the X1.6 flare at 16:53 UT (see Table 1). The orange contour is the integration mask, black contours are PILs. B_z is scaled to \pm 300 G; white (dark) represents positive (negative) values. J_z is scaled to \pm 55 mA m⁻²; green (purple) colors show positive (negative) values. Bottom left: Map of magnetic shear. Shear at pixels within the flare mask with field strengths above 300 G is shown; PILs are shown by black contours. Bottom right: PIL pixels within the mask and with field strengths above 300 G, used to obtain the average PIL shear angle.

Appendix). Pixels within the mask are set to 1, while pixels outside are set to zero. The ratio |DC/RC| is then calculated using only pixels inside the mask, with field strengths larger than 300 G, i.e., 3σ of the noise of the vector magnetic-field data (Hoeksema et al. 2014).

As an example, we show in Figure 1 an application to AR 12205. |DC/RC| is calculated by using only pixels that are enclosed by the orange contour (our mask) and have field strengths larger than 300 G. We find |DC/RC| = 3.50 for $B_z > 0$ and |DC/RC| = 2.62 for $B_z < 0$. For comparison, the |DC/RC| ratios obtained when integrating over the whole area shown in Figure 1 are significantly lower, 2.15 for $B_z > 0$ and 1.68 for $B_z < 0$.

2.3. Calculation of PIL Magnetic Shear

In order to estimate the magnetic shear along an eruptive PIL segment, we calculate the average magnetic shear angle, θ . To this end, we first locate the relevant PIL in the B_z magnetogram. We then compute θ by averaging the shear over the pixels along the PIL, using only pixels that are within the mask and have field strengths of more than 300 G. The shear angle is defined here as the angle between the horizontal component of the potential field and the observed field, as suggested by Hagyard et al. (1984). Large angles imply a high magnetic shear.

For our example case in Figure 1, the bottom left panel shows the shear in the area enclosed by the flare mask, while the bottom right panel shows the pixels used to compute the average PIL shear for this case. It can be seen that those pixels coincide well with the locations of strong current densities (see top right panel) and with areas of large shear. For this case, we find an average shear angle of 75°.

3. Results

The pre-eruptive |DC/RC| ratios and PIL shears for our 28 events are listed in Table 1. Column 1 lists the NOAA number of

the ARs; Column 2 shows the date and time of occurrence (onset time) of the selected flares; Column 3 denotes the flare magnitude and whether or not the flares were associated with CMEs: Column 4 gives the AR position when the flare occurred; Columns 5 and 6 show |DC/RC| computed with our mask method from pixels within positive and negative AR polarities, respectively; Column 7 shows the average value of these computations; Column 8 lists the PIL shear; and Column 9 denotes whether or not an elongated direct current (EDC) bracketing a significant fraction of the eruptive PIL segment could be observed (see, e.g., top right panel in Figure 1). The errors in Columns 5, 6, and 8 are estimated based on the uncertainty of the HMI vector magnetic-field strength, which is 100 G (Hoeksema et al. 2014). For the mean |DC/RC| in Column 7, the error estimation is not straightforward, since the respective |DC/RC| values are obtained in different polarities of B_r . Moreover, in some cases, the difference between those two values is relatively large and the respective absolute errors are relatively small, while in other cases it is the other way around. To provide a conservative estimate for each case, we calculate (i) the error via propagation of the absolute errors of $|DC/RC|^+$ and $|DC/RC|^-$ and (ii) the standard deviation of |DC/RC|, and use the respective larger number as our error estimate. The determination of the EDC is based entirely on visual inspection (of the J_z maps) and therefore somewhat subjective. Ambiguous cases, where clear direct-current concentrations are present but either extend only along relatively small fractions of the eruptive PIL segment or change signs along the segment, are denoted by a question mark.

For the 12 X-class eruptive flares in Group 1, the |DC/RC| value (averaged over the two polarities) prior to the eruptions ranges between 2.3 and 7.0, with an average of 3.6. For the six weaker eruptive flares in Group 2, the values range from 1.6 to 3.5, with a significantly lower average of 2.4. For the 10 confined flares in Group 3, we find |DC/RC| values between 1.0 and 5.4, with an average of 2.2. The CME-producing source regions (Groups 1 and 2) had relatively strong net currents prior to the eruption, with the |DC/RC| ratio tending to be larger for stronger eruptive flares, as shown in Figure 2. We discuss in Section 3.1 how the |DC/RC| values change if the area method (instead of the mask method) is used for the current integration. The PIL shear is typically very large for the cases in Group 1, ranging from 61° to 81°, with an average of 71°. For Group 2, we find values between 46° and 70°, with a smaller average of 59° (note that for two cases the shear could not be measured; see Section 2.1). For the confined flares in Group 3, the shear ranges between 26° and 76°, with a significantly smaller average of 46°. We discuss the quantitative relation between |DC/RC| and PIL shear further in Section 3.2.

Some of the ARs listed in Table 1 contributed both a confined and an eruptive flare to our sample. We discuss those cases in more detail in Section 3.3.

Table 1 shows that almost all source regions of the 12 eruptive X-class flares in Group 1 are characterized by an EDC, with only two (ambiguous) exceptions. This is different in Groups 2 and 3, where we find six cases with an EDC, five cases without, and five ambiguous cases. Tendentiously, the source regions without an EDC are those with the lowest shear in each group. The relationship between EDCs and the PIL shear is further examined in Section 3.4.

An unusual case we encountered was an X-class flare that originated from a PIL segment that was characterized by weak fields ($<300\,\mathrm{G}$) and the absence of significant direct-current

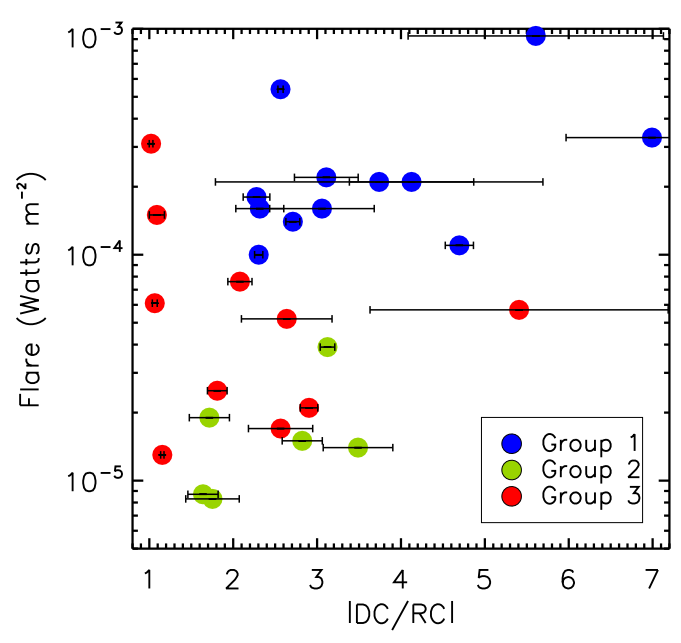


Figure 2. Flare peak (y-axis) vs. |DC/RC| (x-axis) for the events listed in Table 1.

signatures bracketing the PIL, contrary to the clear trend seen in Table 1 for Group 1. We describe this event in Section 3.5 and suggest a possible explanation.

3.1. Comparison of Current-integration Methods

Figure 3 shows a comparison of the |DC/RC| values obtained by using two different methods for determining the area within which the J_z values are integrated. The x and y axes show |DC/RC| computed from the area method and the mask method described above, respectively. The solid black line marks the points where both methods would produce the same result. For all source regions of eruptive flares, the mask method yields a |DC/RC| value that is larger than the one obtained with the area method. For some strong eruptive flares (blue dots) and confined flares (red dots), the number is even more than 2 times larger. The differences are less pronounced for weaker eruptive flares (green dots) and for most confined events, especially for source regions that are well neutralized.

As discussed above and in Liu et al. (2017), the underlying reason for this discrepancy is that the area method typically includes substantial current-carrying magnetic flux that is not involved in the eruption and, therefore, irrelevant to our purpose. This effect is particularly relevant for complex, multipolar ARs that harbor several (potentially closely packed) filament channels. Such channels may have different handedness (i.e., different sign of J_z for the same sign of B_z), leading to a significantly smaller |DC/RC| value. For example, AR 12027 produced a C8.3 flare associated with a CME (see Table 1). The mask method gives a relatively large |DC/RC| = 1.75, as expected. However, the area method yields only |DC/RC| = 1.16, in this case falsely implying that the currents in the eruptive area are almost neutralized. The discrepancy is typically more pronounced the larger the integration area is chosen. For example, for the X2.1 eruptive flare in NOAA AR 12297 (see Table 1), we find |DC/RC| = 3.74 with the mask method and |DC/RC| = 2.82 with the area method, while Qiu et al. (2020) obtained only $|DC/RC| \approx 1.4$ considering the whole AR area. The inclusion of irrelevant current-carrying

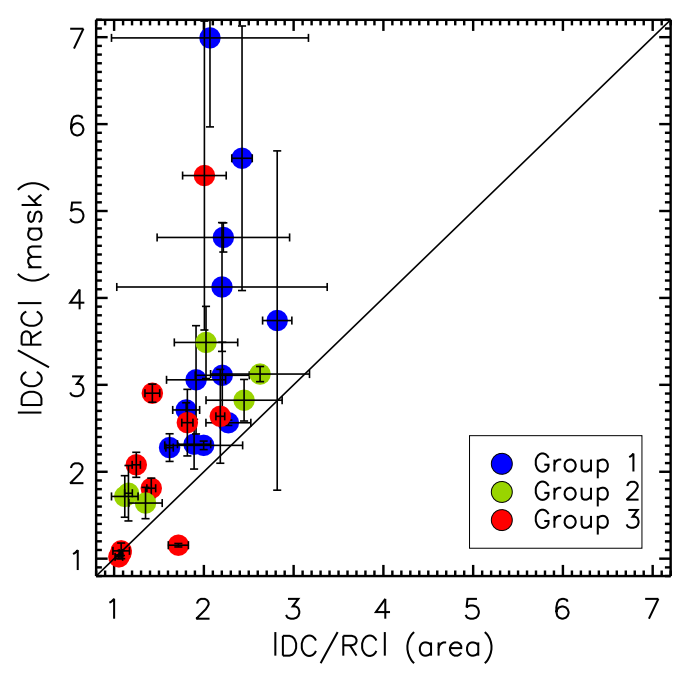


Figure 3. Scatter plot of |DC/RC| computed for our sample of eruptive events shown in Table 1, using a rectangular integration area that encloses the flare region ("area method," *x*-axis) and an area determined from a *Q*-map ("mask method," *y*-axis). Blue, green, and red dots mark the flares from Groups 1, 2, and 3, respectively; respective uncertainties are shown in black.

flux can also artificially increase |DC/RC| (although we found only one such case), as can be seen in the top panels of Figure 5 below. Here the source region of the confined eruption (orange contours) has no pronounced net currents (|DC/RC| = 1.12), but to the east of it there is an EDC, the presence of which yields a |DC/RC| value significantly larger than unity if the area method is used and the EDC is included. These examples suggest that, for a more accurate assessment of the ability of a certain source region to produce a CME, the mask method is highly preferable.

3.2. Current-neutralization Ratio versus PIL Shear

Figure 4 shows |DC/RC| versus PIL magnetic shear for all of our events, except for two cases in Group 2, where too few PIL pixels above 300 G were present to obtain a representative shear value. We can see that the PIL shear increases with increasing |DC/RC|, at least up to |DC/RC| \approx 3, above which it stays more or less similar, within a range of (63–81)°. This is in good agreement with the results by Kazachenko et al. (2022b), who found a strong correlation between |DC/RC| in the cumulative flare-ribbon area and the mean PIL shear, with their largest |DC/RC| value being 2.8. As mentioned above, |DC/RC| and the PIL shear both tend to increase as we go from confined flares to strong eruptive ones, with average values of 2°.2, 2°.8, 3°.6 and 46°, 59°, 71° for Groups 3, 2, 1, respectively.

As discussed in Section 1, Liu et al. (2017) suggested that |DC/RC| may be better suited than the PIL shear for assessing the ability of a source region to produce a CME (versus merely a confined flare). Based on our larger sample, we can now attempt to evaluate the respective success rates of these two quantities. Let us take, for example, the lowest values of the

⁶ Here the average value of |DC/RC| for Group 2 is calculated after removing the two events for which the PIL shear could not be obtained.

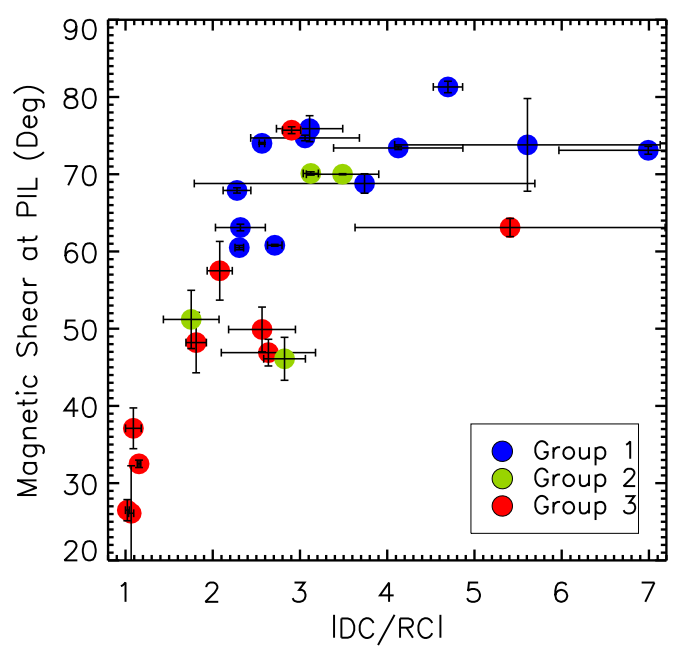


Figure 4. PIL magnetic shear (*y*-axis) vs. |DC/RC| (*x*-axis). The shear is computed using the pixels on the PILs that are enclosed by the mask, whereas |DC/RC| is calculated using all pixels within the mask (see text for details). The colored dots are as in Figure 3. Note that two events from Group 2 are not plotted, due to the lack of shear measurements. Their |DC/RC| values are 1.64 and 1.75, respectively.

PIL shear and |DC/RC| in Group 1 as thresholds. For a PIL shear of 60°, we then find 8 out of 10 (80%) confined flares below that value and 14 out of 16 (88 %) eruptive flares above it, as well as a probability of 88 % for any event above the threshold to be eruptive (neglecting here for the latter that the total numbers of confined and eruptive events are different in our sample). Similarly, if we take |DC/RC| = 2.2, we find 6 out of 10 (60 %) confined events below that value and 15 out of 16 (94 %) eruptive events above it (15 out of 18 [83 %] if we include the two unknown-shear cases from Group 2), as well as a CME probability of 79 %. These numbers are similar to those found previously for other discriminators between confined and eruptive flares (e.g., Li et al. 2022, which was based on a much larger sample) and CME probability (e.g., Falconer et al. 2008). For our sample, the PIL shear "performs" slightly better than |DC/RC|, which is opposite to the suggestion by Liu et al. (2017), namely, that |DC/RC| may be a better proxy for assessing the ability of an AR to produce a CME than the PIL shear.

Figure 4 also reveals a relatively isolated subgroup of four confined events on the bottom left. The source region with the largest PIL shear (in AR 11166; see bottom panels in Figure 6) is a peculiar case, which we discuss in Section 3.3. The remaining three source regions (in ARs 12192 (Figure 8; top), 12222, and 12422 (Figure 5; top)) are all characterized by a |DC/RC| value close to unity, an exceptionally low average PIL shear of 32° or less, and the absence of a clear EDC signature along the eruptive PIL segment(s). While it needs to be evaluated for a larger sample of such cases, this *may* suggest that source regions with these properties often do not contain a well-developed current channel (i.e., a coherent SMA or MFR) and are, therefore, unlikely to produce a CME (though see Section 3.5).

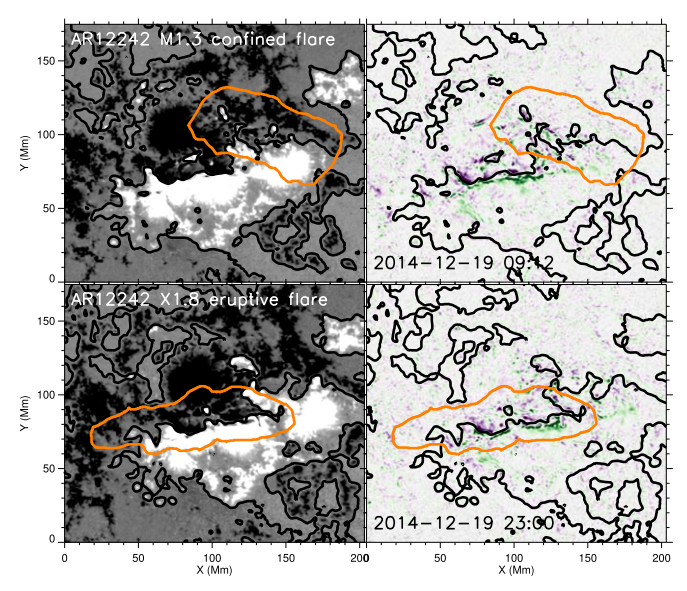


Figure 5. Same as the top panels in Figure 1, here for AR 12242 at 09:12 UT on 2014 December 19, before an M1.3 confined flare that started at 09:31 UT (top), and at 23:00 UT on 2014 December 19, before an X1.8 eruptive flare that started at 00:11 UT on December 20 (bottom).

Indeed, none of the confined flares from our sample that occurred in these three source regions showed indications of a failed filament eruption, i.e., they were all of "Type I," according to the definition by Li et al. (2019). Those authors define "Type I" confined flares as events where the core flux (often outlined by a filament) remains stable during the eruption, and the flaring activity is caused by reconnection, presumably occurring at the location of one or more QSLs that surround the core flux. On the other hand, "Type II" events are caused by the eruption of the core flux, which is then halted by a strong strapping field (e.g., Ji et al. 2003). On the other hand, a filament was clearly visible along the whole eruptive PIL segment of AR 12222 prior to the eruption, suggesting the presence of an SMA or MFR carrying the filament material. Furthermore, Duan et al. (2019), who performed NLFFF extrapolations for a large sample of pre-eruptive configurations (including 18 of our cases), found an MFR above the eruptive PIL segments in ARs 12222 and 12192, suggesting that a preeruptive current channel was present in these two cases, even though it may not have been directly involved in the respective eruptions.

All other source regions of confined flares in our sample have a PIL shear of at least 46° and a |DC/RC| value of at least 1.7, and most of them exhibit an EDC. This suggests the presence of a well-developed current channel (e.g., Patsourakos et al. 2020) and, therefore, in principle, the ability of the source region to produce a CME. For such regions, quantities obtained from photospheric measurements, such as |DC/RC| or PIL shear, do not seem to be sufficient to fully assess the nature of eruptions (confined or CME) that may occur in the region. Despite an overall tendency of these values to be larger for CME-producing regions (see Section 1), there exists a considerable overlap (see Figure 4). Additional information about the properties of the ambient strapping field, such as the "decay index" (e.g., Kliem & Török 2006), would be needed to

We note that we disagree here with Li et al. (2019), who classified the M6.1 confined flare from AR 12222 as "Type II". Our visual inspection of the event did not reveal any clear signatures of a Type II eruption.

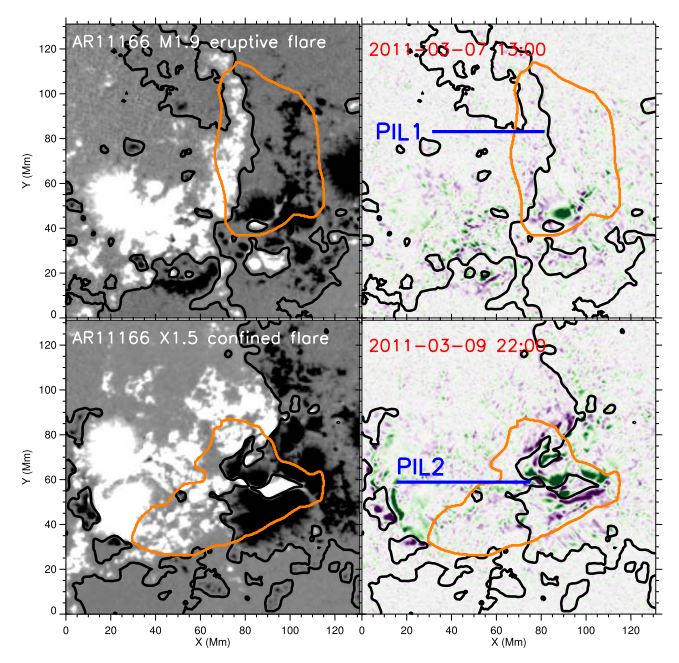


Figure 6. Same as the top panels in Figure 1, here for AR 11166 at 13:00 UT on 2011 March 7, before an eruptive M1.9 flare that started at 13:45 UT (top), and at 22:00 UT on 2011 March 9, before a confined X1.5 flare that started at 23:13 UT (bottom). The PIL segments that are involved in the two events are marked with "PIL1" and "PIL2," respectively. The magnetic field evolved dramatically during this two-day time period.

improve the predictive capabilities evaluated above. For first attempts in this direction, see, e.g., Duan et al. (2019), as well as Li et al. (2022), who used the unsigned AR flux instead of the decay index.

3.3. ARs with Eruptive and Confined Flares

Three ARs in our sample produced both confined and eruptive events, and we briefly describe those cases here. AR 12242 produced a confined M1.3 flare at 09:31 UT on 2014 December 19, and an eruptive X1.8 flare at 00:11 UT on 2014 December 20. The two events occurred at different locations (i.e., PIL segments) in the AR, as shown in Figure 5, suggesting that two separate flux systems were involved. The source region of the eruptive flare had |DC/RC| = 2.28, an average PIL shear of 68° and a clear EDC signature. On the other hand, the source region of the confined flare, which belongs to the "subgroup" discussed in the previous section, had |DC/RC| = 1.16, 33° PIL shear, and no EDC. This reiterates that source regions of eruptions can have very different properties even within a single AR and that one should therefore restrict the current integration to the area of relevant flux. Indeed, when using the area method for the current integration, we find that |DC/RC| is almost the same for the two events: 1.62 for the eruptive flare and 1.72 for the confined one.

AR 11166 produced an eruptive M1.9 flare at 13:45 UT on 2011 March 7, and a confined X1.5 flare more than two days later, at 23:13 UT on 2011 March 9 (see Li et al. 2019 for a detailed description of the latter event). The AR evolved dramatically during this time period, including the emergence of magnetic flux, pronounced motion of magnetic patches, and a significant change in the distribution of the PILs (see Figure 6). The eruptive flare was associated with PIL 1 (top panels), and the relevant source region had |DC/RC| = 1.72, 51° PIL shear, and no EDC. After the flux emergence and evolution of the AR, a

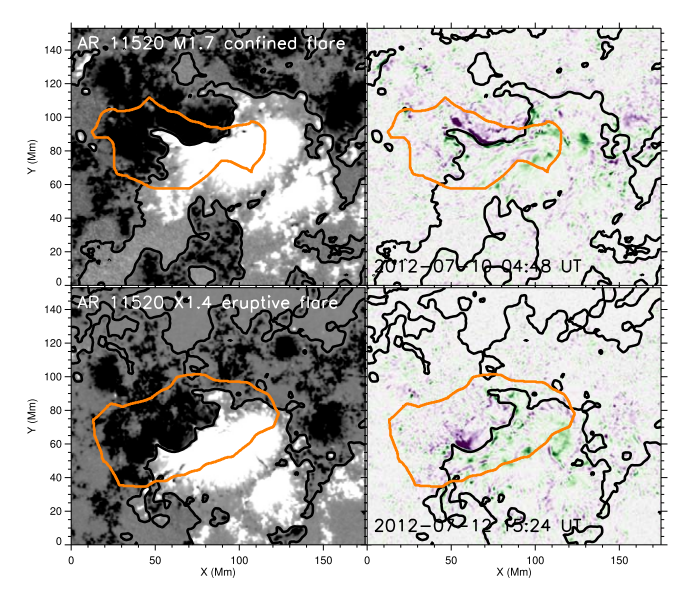


Figure 7. Same as the top panels in Figure 1, here for AR 11520 at 04:48 UT on 2012 July 10, before an M1.7 confined flare that started at 04:58 UT (top), and at 15:24 UT on 2012 July 12 before an X1.4 eruptive flare that started at 15:37 UT (bottom).

new PIL enclosing a positive parasitic polarity was formed (PIL 2; bottom panels), which was at the heart of the confined flare. Interestingly, despite the presence of strong currents surrounding the PIL, we found only a relatively low PIL shear of 37° and a very low |DC/RC| = 1.09. A closer look at the J_{z} distribution reveals closely packed current patches of opposite signs within each of the polarities surrounding PIL 2, and the same can be seen along the highly curved PIL segment north of the parasitic polarity. This implies the presence of several independent current systems of different helicity signs within the eruptive area (Li et al. 2019 mention three separate filaments), as opposed to the single-handedness EDCs typically seen in our sample. For this reason, we marked the EDC as "ambiguous" in Table 1 for this event. In this particular case, the eruption spread over an area that contained several current systems of opposite handedness, whose contributions in the current integration largely canceled out, so the |DC/RC| value close to unity is likely misleading and should be taken with some care.

AR 11520 produced a confined M1.7 flare at 04:58 UT on 2012 July 10 and an eruptive X1.4 flare at 15:37 UT on 2012 July 12, i.e., about 2.5 days apart. In contrast to the two cases described above, the flares occurred at roughly the same location, associated with the same PIL segment, whose shape evolved to some degree during the two days, but not dramatically (see Figure 7). We find |DC/RC| = 2.57 and 2.71 for the two events, respectively. The PIL shear is 50° for the confined event and 61° for the eruptive one, i.e., not very different either. Both source regions display an EDC, with the one preceding the confined event being somewhat more pronounced. This case nicely illustrates that, for a better distinction between eruptive and confined events, information on the strapping field should be included (see Section 3.2).

3.4. Elongated Direct Currents and Sheared PILs

As mentioned at the beginning of this section, almost all source regions of our eruptive X-class flares exhibited an EDC, while the source regions of the weaker eruptive and the confined flares had an EDC only in about half of the cases. One has to

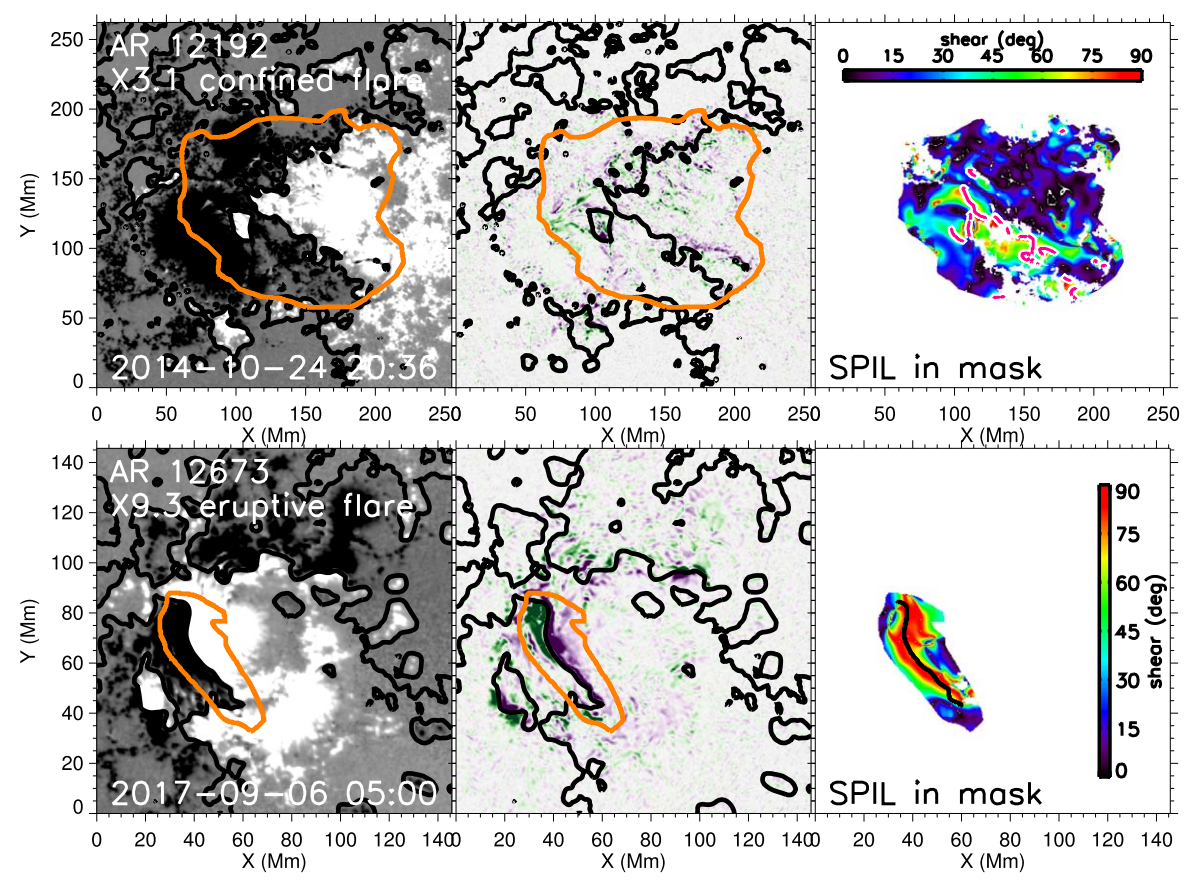


Figure 8. Example of a highly fragmented SPIL (top; AR 12192) and of a continuous SPIL (bottom; AR 12673). Both ARs are shown shortly before the respective flare times given in Table 1. The left and central panels are as in earlier figures; the right panels show, within the respective current-integration areas, the SPILs (PIL areas with field strengths above 300 G and shear angles above 45°) as thick magenta (top) and black (bottom) contours, together with the corresponding shear maps (see bottom left panel in Figure 1).

keep in mind, though, that the absence of clear EDC signatures at the observed photospheric level does not rule out the presence of a pre-eruptive MFR higher up in the atmosphere and, hence, the principal ability of the source region to produce a CME. We discuss such a case in detail in the next section.

The presence of a clear EDC in our sample is associated with large |DC/RC| values of at least 2.1 and a PIL shear of at least 46°. Investigating a sample of 20 ARs, Vemareddy (2019) found that SPILs (PIL segments with a shear angle larger than 45°) are relatively fragmented in source regions of confined flares, while they are much more coherent in source regions of CMEs. We find the same trend in our sample, i.e., more fragmented SPILs for confined events (especially for the subgroup described in Section 3.2) and more coherent, elongated SPILs for eruptive ones (for those cases where the PIL shear could be reliably determined). The latter typically coincide very well with the respective EDCs, which is not surprising, as both SPILs and EDCs are most likely signatures of a well-developed current channel (i.e., an MFR or SMA; e.g., Patsourakos et al. 2020). Figure 8 shows an example of a source region with fragmented SPILs producing a confined flare (from the subgroup) and an eruptive flare associated with a continuous SPIL.

3.5. Strong Eruptive Flares without EDCs

While the source regions of the strong (X-class) eruptive flares in our sample are typically characterized by an EDC (and

a co-spatial SPIL), some strong eruptive flares are not associated with such signatures. Moreover, such eruptions may stem from areas of relatively weak fields ($\lesssim 300\,\mathrm{G}$). An example of such a case is the X1.2 flare that occurred on 2014 January 7 at the periphery of AR 11944 and was associated with a very fast CME (projected speed $\approx 2400\,\mathrm{km\,s^{-1}}$, e.g., Möstl et al. 2015).

A possible explanation for the absence of an EDC (or any pronounced direct-current signature along the PIL) is that the current-carrying, pre-eruptive flux is largely located in the (low) corona and therefore escapes detection. In order to check this for the 2014 January 7 event, we performed an NLFFF extrapolation of the AR and its surroundings.

Figure 9(a) shows the pre-processed magnetogram (obtained from HMI vector data) shortly before the X1.2 flare. The eruptive PIL segment is located between the western positive-polarity sunspot of the AR and an area of already relatively dispersed negative flux next to the AR. We found no pixels with strengths above 300 G along this segment, which is why we did not include this case in our sample.

Figure 9(b) shows that no EDC is present along the eruptive PIL segment. However, the extrapolation reveals an EDC at coronal heights, whose strength is comparable to those of the currents in the adjacent sunspot at the same height (Figure 9(c)). Field lines drawn at the location of this current pattern show that the current flows along an MFR that connects the southern edge of the sunspot with the negative-polarity area (Figure 9(d)). A side view on the MFR shows that, indeed, a considerable fraction

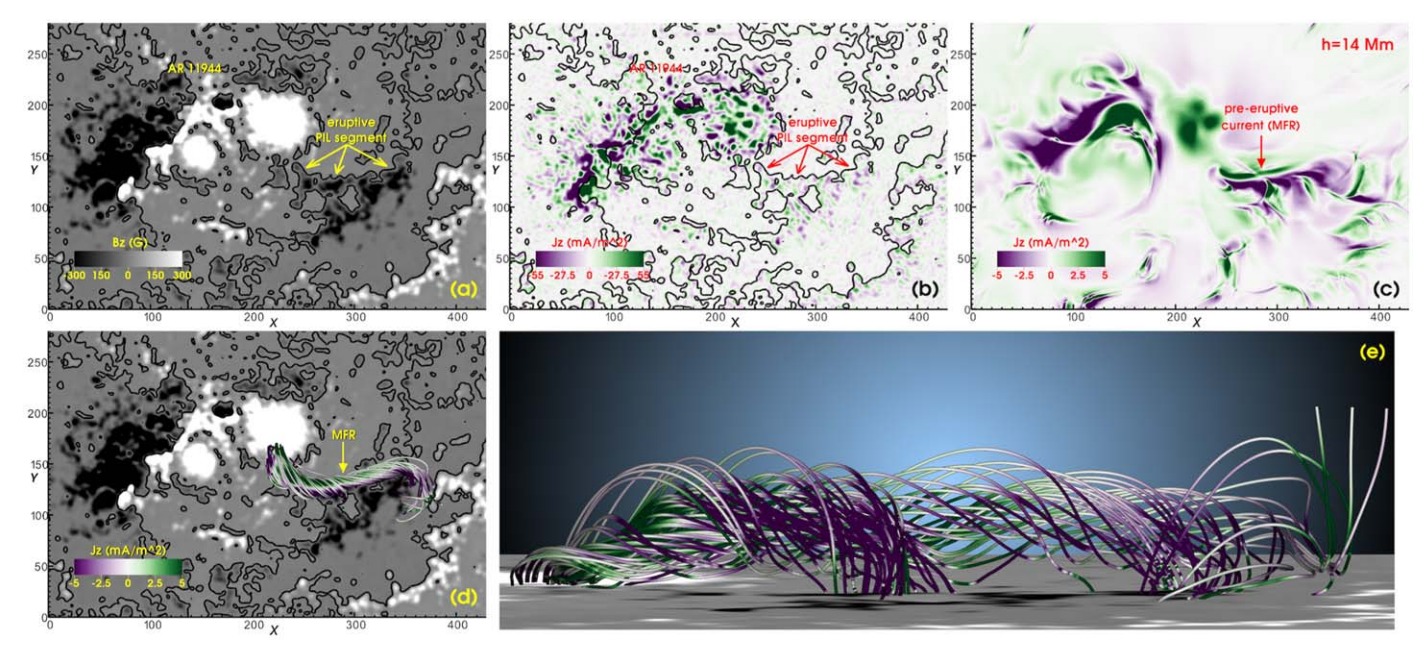


Figure 9. NLFFF extrapolation of AR 11944, shortly before the X1.2 flare on 2014 January 7. (a) Pre-processed magnetogram used for the extrapolation. The eruption occurred above a PIL at the periphery of the AR (indicated by arrows). (b) J_z at the photosphere. No pronounced direct-current concentrations are visible along the eruptive PIL segment. (c) J_z at a height of 14 Mm. An elongated direct-current concentration is present above the eruptive PIL segment at this height. (d) Same as (a), showing an MFR that corresponds to the pre-eruptive current in (c). Field lines are colored by J_Z . (e) Side view on the MFR, showing that most of its flux is located above the surface.

of its flux arches into the corona (Figure 9(e)), with connections to the surface that coincide with localized J_z signatures at the photosphere but do not display a coherent pattern, i.e., an EDC.

At this point, we can only speculate as to why this preeruptive configuration was different from the source regions of most of the eruptive X-class flare cases in Group 1. One characteristic property of this source region was that the eruptive PIL segment was located at the periphery of the AR, between a strong sunspot and an already dispersed flux concentration, rather than within the AR itself. The same was true for the source regions of the eruptive X-class flare in AR 12158, the eruptive C- and M-class flares in ARs 11667, 11305, and 12027, for the confined M-class flare in AR 12242, and, to some degree, for the confined flare M-class flare in AR 12268—none of these source regions exhibited a clear EDC. On the other hand, the CME-producing source regions in our sample where the eruptive PIL was located between the main AR polarities typically exhibited an EDC/SPIL. This may suggest that the formation mechanism and resulting properties of filament channels that develop between a sunspot (or newly emerging flux) and an older, already dispersed flux region (e.g., Gaizauskas et al. 1997) may be somewhat different from the mechanism(s) forming such channels between main AR polarities. This question requires further investigation that is beyond the scope of the work presented here.

4. Summary and Discussion

In this article we presented a detailed investigation of the degree of current neutralization in eruptive solar ARs, extending our previous study Liu et al. (2017). The degree of current neutralization was quantified by the ratio of the total direct current and the total return current in the photosphere, |DC/RC|, within the area of eruptive flux, as estimated from Q

maps calculated using NLFFF extrapolations and from EUV observations of flare ribbons and arcades. Following Liu et al. (2017), the main purpose of our investigation was to test, for a significantly larger sample, whether |DC/RC| constitutes a suitable proxy for assessing whether or not an AR has the ability to produce a CME and to compare its efficiency to other potential proxies, here specifically to the amount of the magnetic shear along the eruptive PIL segment.

To this end, we considered a sample of 28 flares that occurred between 2011 February and 2017 September, and for which suitable AIA observations and HMI vector data were available. The sample was grouped into strong (X-class) eruptive flares (i.e., flares associated with a CME; 12 cases), weaker eruptive flares (6 cases), and confined flares (without a CME; 10 cases). We also tested how the choice of the area used for the integration of the current densities affects the resulting |DC/RC| value. In particular, we compared our "mask method" to the "area method" most commonly used in similar studies. Finally, we discussed specific cases for which the calculation of |DC/RC| and the interpretation of the results requires additional considerations. The main results of our investigation can be summarized as follows.

(1) We demonstrated, for a significantly larger sample than used in Liu et al. (2017), that calculating the degree of current neutralization by merely selecting a rectangular area around the source region of an eruption or an entire AR ("area method") can strongly underestimate the |DC/RC| value that is physically relevant for an observed (or potentially occurring) eruption. Overall, the |DC/RC| values we find for our sample are substantially larger than those reported in similar investigations (Vemareddy 2019; Avallone & Sun 2020; He et al. 2020; Kazachenko et al. 2022b).

Therefore, whenever possible, the more accurate "mask method" (or any other method that approximates the region of

the actual or potentially erupting flux) should be used, as we did in this investigation. If the (less time-consuming) area method is used, the integration area should be restricted as close as possible around the erupting flux, especially for complex ARs where several current systems may be present. This is particularly important if the normal components of the respective direct currents have opposite signs within areas of the same magnetic polarity, as their contributions may largely cancel out if a common integration area is used, falsely suggesting current neutralization. Further investigations with larger samples should reveal whether the "area method" may be sufficient for practical purposes. We note that here we employed NLFFF extrapolations to determine the area of erupting flux. In principle, potential-field extrapolations can be used for this purpose as well, but it must be kept in mind that such a field may provide an inferior approximation of the area of eruptive flux if strong currents are present in the source region, as the fields produced by those currents will be neglected.

(2) All CME-producing source regions in our sample have relatively strong net currents prior to the eruption (|DC/RC| > 1.63), tending to be larger for stronger flares (|DC/RC| > 2.27 for X-class flares), with a total range of 1.6–7.0 and an average value of 3.2. On the other hand, in source regions of confined events, |DC/RC| ranges between 1.0 and 5.4, with an average value of 2.2. Similarly, for the PIL shear, we find a range of (46–81)° for source regions of CME-producing events, with an average of 68°, and a range of (26–76)° for source regions of confined events, with an average value of 46°. Evaluating the ability of both quantities to assess whether a source region produces a CME or a confined eruption, we find that the PIL shear performs slightly better than |DC/RC| and that both perform similarly to previously used discriminators (see Section 3.2).

(3) Source regions with |DC/RC| values significantly above unity are characterized by the presence of pronounced direct currents located close to the eruptive PIL. These direct currents are often relatively elongated (EDCs), bracketing a substantial fraction of the eruptive PIL, and typically co-spatial with coherent, highly sheared PIL segments (SPILs). For the 16 source regions in our sample that exhibited a clear EDC, we found large |DC/RC| values of at least 2.1 and a PIL shear of at least 46°.

EDCs and coherent SPILs are most likely signatures of the presence of a well-developed current channel, i.e., an MFR or SMA, a pre-requisite for the occurrence of a CME (e.g., Patsourakos et al. 2020). In CME-producing source regions where no clear EDC or SPIL is observed, the pre-eruptive MFR or SMA may partly extend into the corona and therefore escape detection at the photospheric level, as we demonstrated for one case in Section 3.5.

(4) We found four source regions with |DC/RC| very close to unity (1.02–1.16), all of which produced confined flares and appear somewhat separated from the rest of the sample (see Figure 4). Apart from one peculiar case, these regions were characterized also by a very low PIL shear (below 33°) and the absence of a clear EDC signature. At first glance, these properties seem to suggest that no well-developed current channel was formed in the source region and that, therefore, a CME is likely not imminent. However, as discussed in Section 3.2, NLFFF extrapolations suggest the

presence of an MFR above the eruptive PIL segment for two of these three cases. Larger samples of such source regions are needed to test to what extent the above properties may be used to predict whether a potential eruption will indeed be confined.

On the other hand, the six remaining source regions that produced confined flares in our sample |DC/RC| ranged between 1.8 and 5.4, with an average value of 3.0, while the PIL shear range was $(47-76)^{\circ}$, with an average value of 57° . These numbers are somewhat smaller but still comparable to those found for our CME-producing source regions. This is an inherent limitation of either proxy to assess whether a potential eruption will produce a CME or will remain confined. This is simply because both |DC/RC| and the PIL shear merely contain information about the pre-eruptive current channel, but not about the ambient/overlying field, which may determine to a large extent the evolution of an eruption (e.g., Török & Kliem 2005). To improve this, proxies such as |DC/RC| or PIL shear should be combined with quantities that characterize the properties of the ambient/overlying magnetic field into which a potential eruption would evolve, such as the "decay index" (e.g., Kliem & Török 2006; Duan et al. 2019) or the unsigned AR flux (e.g., Li et al. 2022).

Overall, our investigation suggests that the quantity |DC/RC| is comparably well, but not better, suited for assessing the ability of ARs to produce CMEs than the amount of PIL shear or other proxies (see Section 3.2), which is contrary to the aspiration expressed in Liu et al. 2017, who considered only one confined-event source region (AR 12192) that belongs to the subgroup of source regions with |DC/RC| close to unity discussed in Section 3.2. The reason for this equivalence of |DC/RC| and PIL shear is the (apparent) absence of a return current enclosing the direct current in real current channels. Such return currents, whose presence has been occasionally postulated (see, e.g., the Introduction in Török et al. 2014), would decrease the hoop force in the current channel, making a full eruption of the latter less likely (see Liu et al. 2017). Hence, |DC/RC| would contain additional information on potential CME occurrence compared to the mere PIL shear, rendering it a more powerful proxy. However, we did not find any indications for enclosing return currents in our sample, in line with the earlier studies mentioned in Section 1. Indeed, NLFFF models and MHD simulations suggest that such currents do not form (or a relatively weak) in the presence of substantial PIL shear, i.e., in pre-eruptive current channels (Török & Kliem 2003; Török et al. 2014; Dalmasse et al. 2015; Titov et al. 2021).

Acknowledgments

We wish to thank SDO team members who have made great contributions to the SDO mission for their hard work! We thank the anonymous referee for valuable comments and suggestions. This work was supported by NASA's HGIO program (award No. 80NSSC18K0670). The data have been used by courtesy of NASA/SDO and the HMI science team. T.T. acknowledges additional support by NASA's HGIO program (award no. 80NSSC19K0263), NASA's HTMS program (award No. 80NSSC20K1274), NSF's PREEVENTS program (award No. ICER-1854790), and by NRL contract N0017319C2003 to Predictive Science Inc., a subcontract of NASA LWS grant 80HQTR19T0084 to NRL. V.S.T. was

additionally supported by the NASA HSR program (award No. 80NSSC20K1317). Y.L. was supported additionally by the NASA LWS program (award No. 80NSSC19K0072) and NASA contract NAS5-02139 to Stanford University. X.S. acknowledges additional support from NSF's PREEVENTS program (award No. ICER-1854760). M.J. acknowledges NASA's SDO/AIA contract (NNG04EA00C) to LMSAL.

Appendix

In this Appendix we present maps of the vertical magnetic field, B_z , vertical electric current density, J_z , and the squashing factor, Q, for all cases listed in Table 1 (Figures 10–15; shown in the same order as in the table). We refer the reader to the main text for a description of how these quantities were obtained.

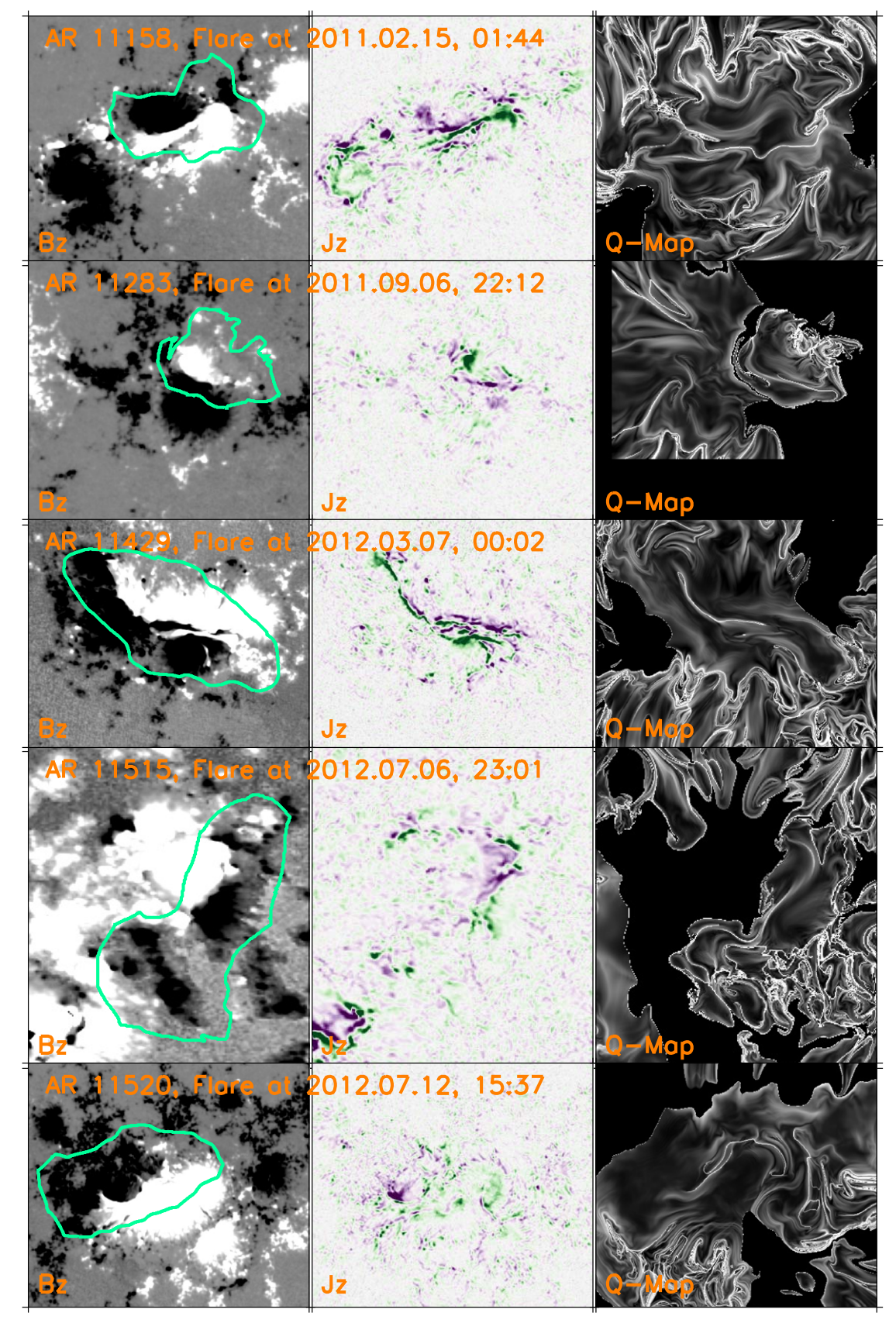


Figure 10. From left to right: Pre-eruptive B_z , J_z , and Q-map for the events listed in Table 1. B_z is scaled to ± 300 G, overplotted in contour (green) by the flare mask; white (dark) represents positive (negative) values. J_z is scaled to ± 55 mA m $^{-2}$; green (purple) and shows positive (negative) values. Q is shown on a logarithmic scale, saturated at Q=4. White colors correspond to high Q values. The AR number and the flare onset time are marked on the top of the images. The green contour in the B_z image shows the mask used for the |DC/RC| calculation (see Section 2.2).

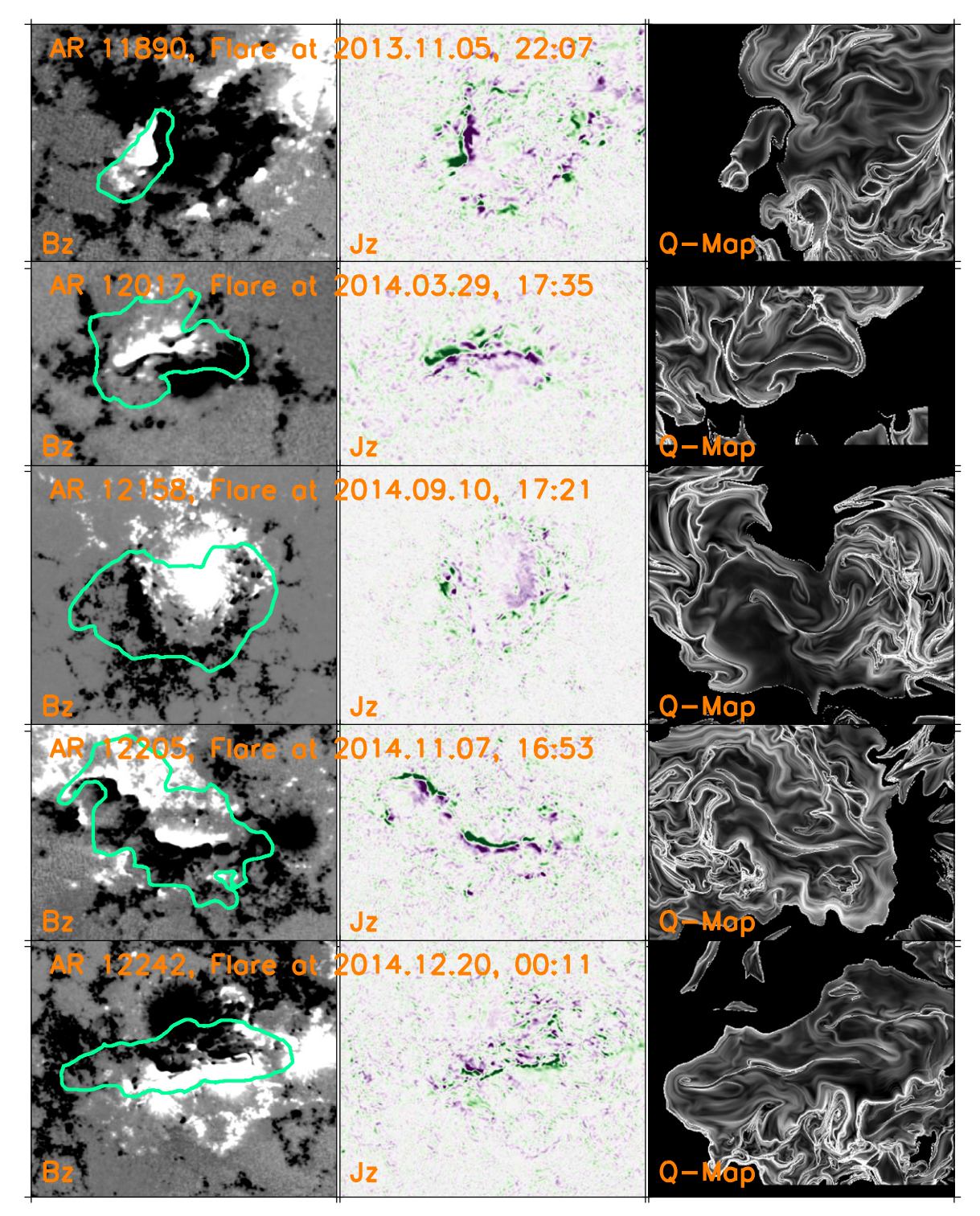


Figure 11. Same as Figure 10 for different cases.

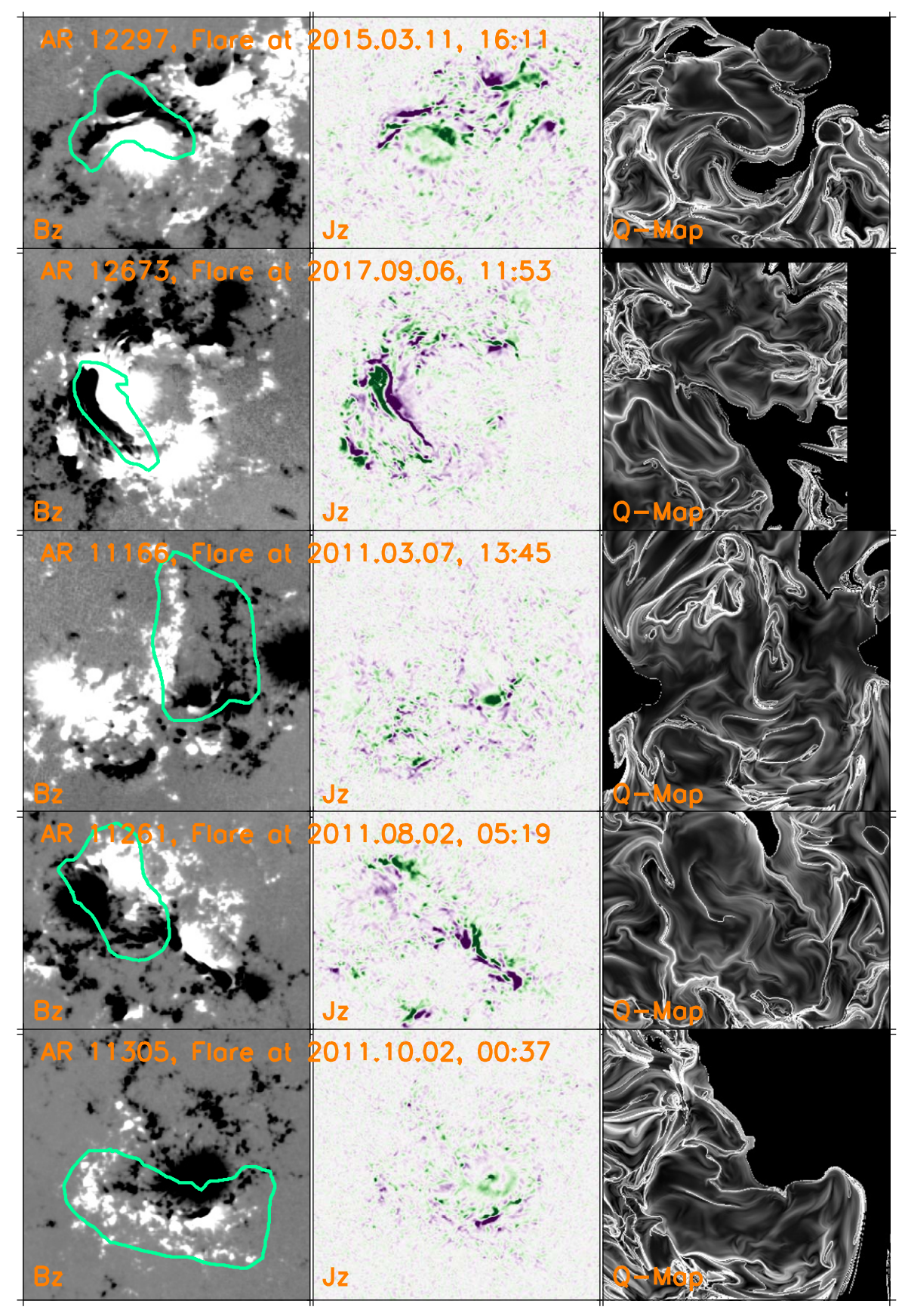


Figure 12. Same as Figure 10 for different cases.

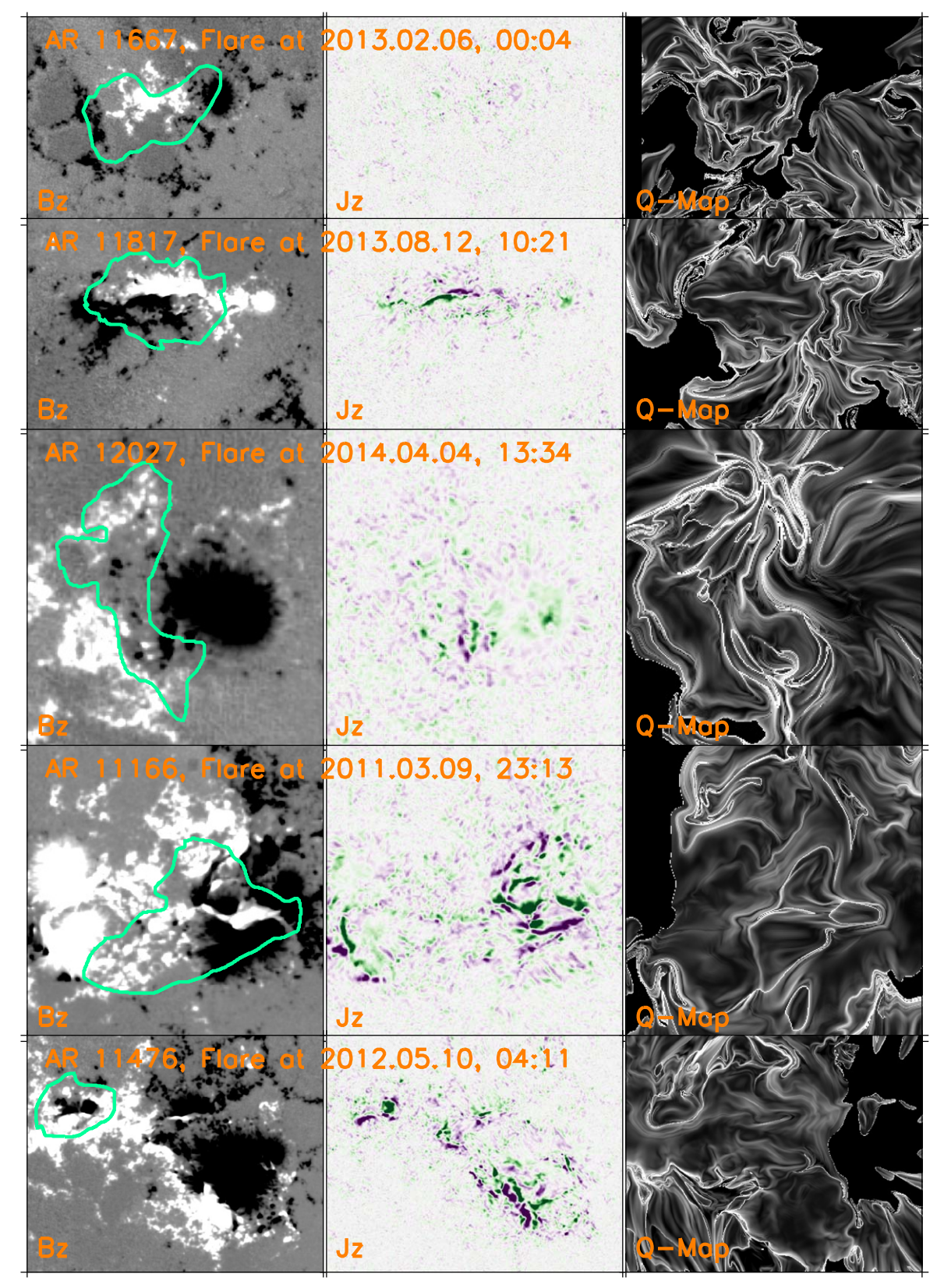


Figure 13. Same as Figure 10 for different cases.

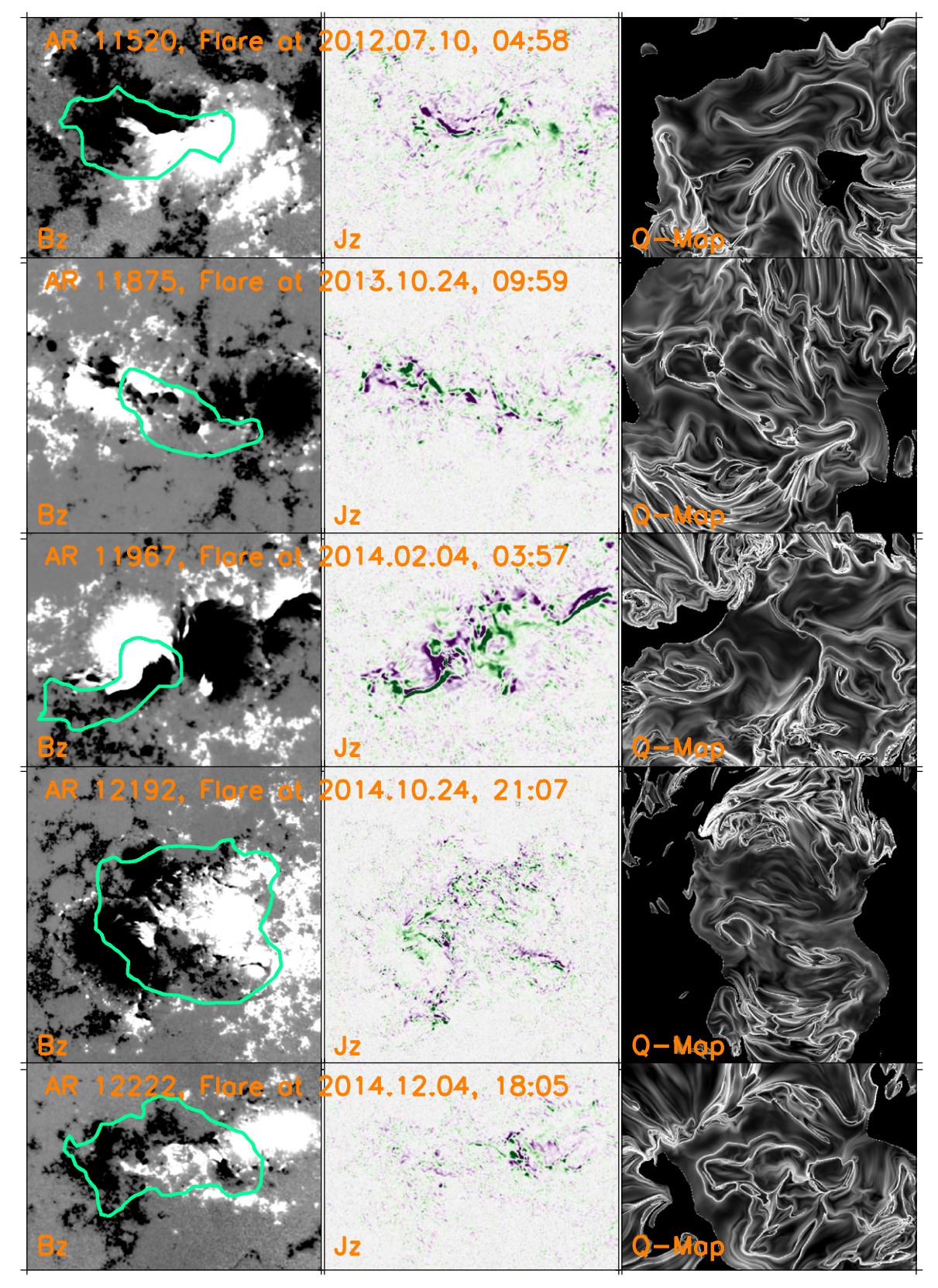


Figure 14. Same as Figure 10 for different cases.

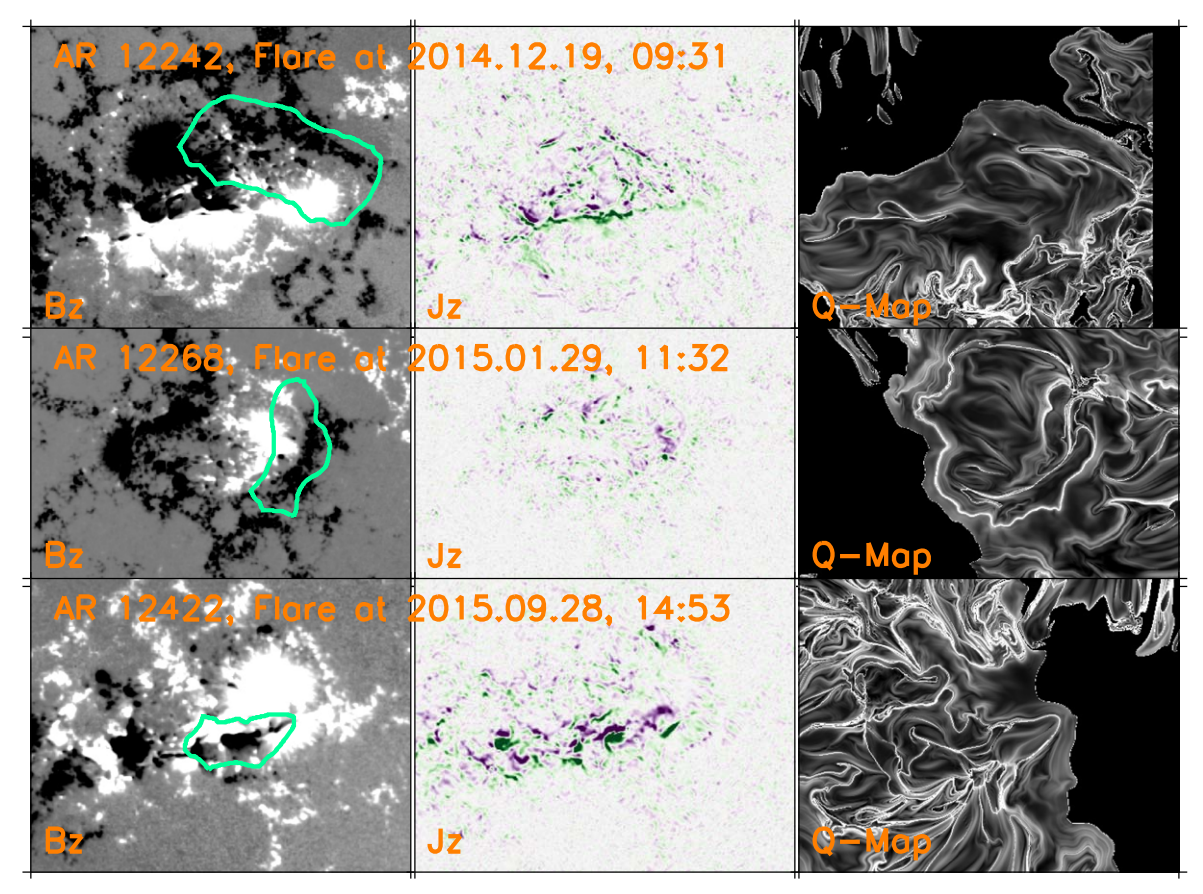


Figure 15. Same as Figure 10 for different cases.

ORCID iDs

Y. Liu ® https://orcid.org/0000-0002-0671-689X
T. Török ® https://orcid.org/0000-0003-3843-3242
V. S. Titov ® https://orcid.org/0000-0001-7053-4081
J. E. Leake ® https://orcid.org/0000-0002-6936-9995
X. Sun (孙旭东) ® https://orcid.org/0000-0003-4043-616X
M. Jin ® https://orcid.org/0000-0002-9672-3873

References

```
Avallone, E. A., & Sun, X. 2020, ApJ, 893, 123
Barnes, G., Leka, K. D., Schrijver, C. J., et al. 2016, ApJ, 829, 89
Bobra, M. G., Sun, X., Hoeksema, J. T., et al. 2014, SoPh, 289, 3549
Borrero, J. H., Tomczyk, S., Kubo, M., et al. 2011, SoPh, 273, 267
Centeno, R., Schou, J., Hayashi, K., et al. 2014, SoPh, 289, 3531
Dalmasse, K., Aulanier, G., Démoulin, P., et al. 2015, ApJ, 810, 17
Demoulin, P., Bagala, L. G., Mandrini, C. H., Henoux, J. C., & Rovira, M. G.
   1997, A&A, 325, 305
Duan, A., Jiang, C., He, W., et al. 2019, ApJ, 884, 73
Falconer, D. A., Moore, R. L., & Gary, G. A. 2008, ApJ, 689, 1433
Forbes, T. G. 2000, JGR, 105, 23153
Gaizauskas, V., Zirker, J. B., Sweetland, C., & Kovacs, A. 1997, ApJ, 479, 448
Georgoulis, M. K., Titov, V. S., & Mikić, Z. 2012, ApJ, 761, 61
Green, L. M., Török, T., Vršnak, B., Manchester, W., & Veronig, A. 2018,
   SSRv, 214, 46
Hagyard, M. J., Smith, J. B., Jr., Teuber, D., & West, E. A. 1984, SoPh,
He, Y., Liu, R., Liu, L., et al. 2020, ApJ, 900, 38
Hoeksema, J. T., Liu, Y., Hayashi, K., et al. 2014, SoPh, 289, 3483
Janvier, M., Savcheva, A., Pariat, E., et al. 2016, A&A, 591, A141
Ji, H., Wang, H., Schmahl, E. J., Moon, Y. J., & Jiang, Y. 2003, ApJL, 595, L135
Kazachenko, M. D., Albelo-Corchado, M. F., Tamburri, C. A., &
   Welsch, B. T. 2022a, SoPh, 297, 59
Kazachenko, M. D., Lynch, B. J., Savcheva, A., Sun, X., & Welsch, B. T.
   2022b, ApJ, 926, 56
```

```
Kliem, B., & Török, T. 2006, PhRvL, 96, 255002
Kontogiannis, I. 2023, AdSpR, 71, 2017
Leka, K. D., Barnes, G., Crouch, A. D., et al. 2009, SoPh, 260, 83
Li, T., Hou, Y., Yang, S., et al. 2020, ApJ, 900, 128
Li, T., Liu, L., Hou, Y., & Zhang, J. 2019, ApJ, 881, 151
Li, T., Sun, X., Hou, Y., et al. 2022, ApJL, 926, L14
Liu, R., Kliem, B., Titov, V. S., et al. 2016, ApJ, 818, 148
Liu, Y., Sun, X., Török, T., Titov, V. S., & Leake, J. E. 2017, ApJL, 846, L6
Longcope, D. W., & Welsch, B. T. 2000, ApJ, 545, 1089
Masson, S., Pariat, E., Aulanier, G., & Schrijver, C. J. 2009, ApJ, 700, 559
Metcalf, T. R. 1994, SoPh, 155, 235
Möstl, C., Rollett, T., Frahm, R. A., et al. 2015, NatCo, 6, 7135
Norton, A. A., Pietarila, G. J., Ulrich, R. K., et al. 2006, SoPh, 239, 69
Patsourakos, S., Vourlidas, A., Török, T., et al. 2020, SSRv, 216, 131
Pesnell, W. D., Thompson, B. J., & Chamberlin, P. C. 2012, SoPh, 275, 3
Qiu, Y., Guo, Y., Ding, M., & Zhong, Z. 2020, ApJ, 901, 13
Ravindra, B., Venkatakrishnan, P., Tiwari, S. K., & Bhattacharyya, R. 2011,
   ApJ, 740, 19
Savcheva, A., Pariat, E., McKillop, S., et al. 2015, ApJ, 810, 96
Scherrer, P. H., Schou, J., Bush, R. I., et al. 2012, SoPh, 275, 207
Schou, J., Scherrer, P. H., Bush, R. I., et al. 2012, SoPh, 275, 229
Schrijver, C. J. 2009, AdSpR, 43, 739
Sun, X., & Cheung, M. C. M. 2021, SoPh, 296, 7
Temmer, M. 2021, LRSP, 18, 4
Titov, V. S. 2007, ApJ, 660, 863
Titov, V. S., Downs, C., Török, T., et al. 2021, ApJS, 255, 9
Titov, V. S., Mikic, Z., Linker, J. A., Lionello, R., & Antiochos, S. K. 2011,
Török, T., & Kliem, B. 2003, A&A, 406, 1043
Török, T., & Kliem, B. 2005, ApJL, 630, L97
Török, T., Leake, J. E., Titov, V. S., et al. 2014, ApJL, 782, L10
Turmon, M., Jones, H. P., Malanushenko, O. V., & Pap, J. M. 2010, SoPh,
   262, 277
Vemareddy, P. 2019, MNRAS, 486, 4936
Vemareddy, P. 2021, FrP, 9, 605
Vemareddy, P., Venkatakrishnan, P., & Karthikreddy, S. 2015, RAA, 15, 1547
Wiegelmann, T. 2004, SoPh, 219, 87
Zhang, J., Temmer, M., Gopalswamy, N., et al. 2021, PEPS, 8, 56
```